AGU PUBLICATIONS

Geophysical Research Letters

RESEARCH LETTER
10.1002/2016GL070345

Key Points:
- We present a framework for fully coupled nonlinear fault and mantle dynamics using the integral method
- Earthquakes and slow-slip events can trigger viscoelastic relaxation, contributing significantly to far-field deformation for large events
- Onset of viscous flow during the early postseismic period, potentially within minutes of the coseismic rupture

Supporting Information:
- Supporting Information S1
- Movie S1

Correspondence to:
V. Lambert,
vlambert@caltech.edu

Citation:
Lambert, V., and S. Barbot (2016), Contribution of viscoelastic flow in earthquake cycles within the lithosphere-asthenosphere system, *Geophys. Res. Lett.*, *43*, 10,142–10,154, doi:10.1002/2016GL070345.

Received 11 JUL 2016
Accepted 15 SEP 2016
Accepted article online 19 SEP 2016
Published online 9 OCT 2016

Contribution of viscoelastic flow in earthquake cycles within the lithosphere-asthenosphere system

Valère Lambert[1] and Sylvain Barbot[1]

[1] Earth Observatory of Singapore, Nanyang Technological University, Singapore

Abstract Faults slip relaxes lithospheric stress imposed by mantle flow and in turn transfers stress to the ductile regions. The interplay of these systems governs the style of deformation at plate boundaries including the recurrence of seismic events. However, such deep processes remain challenging to incorporate in numerical simulations of earthquake cycles. Here we propose a model that couples fault slip and viscoelastic deformation to simulate fault dynamics in the lithosphere-asthenosphere system. Our method resolves all phases of the earthquake cycle, including dynamic rupture propagation, afterslip, slow-slip events, and the modulation of strain rate incurred in the ductile regions. Transient strain accelerations in the asthenosphere may follow both earthquakes and slow-slip events shortly after the rupture, depending on the rheology of the upper mantle and the magnitude of the event. This study opens the door to greater insight into the variability of earthquake cycles by incorporating the dynamics of distributed deformation.

1. Introduction

Solutions for the displacement and stress fields due to faults [*Okada*, 1985; *Okada*, 1992] have been essential to interpret geodetic observations as well as strain and tilt data from deep boreholes. Theoretical and numerical modeling of fault kinematics from geodetic data have enabled an explosion of new findings about the mechanics of the earthquake cycle [e.g., *Ampuero and Rubin*, 2008; *Barbot et al.*, 2009, 2012; *Erickson and Dunham*, 2014; *Hori et al.*, 2004; *Jiang and Lapusta*, 2016; *Kaneko et al.*, 2010, 2011; *Kenner and Segall*, 2000; *Lapusta and Rice*, 2003; *Lapusta and Liu*, 2009; *Segall and Davis*, 1997]. These models have been mostly confined to processes along the interface of a fault, neglecting the inelastic properties of the surrounding volume. Several studies have shown the importance of the mechanical coupling between the brittle and ductile regions in the context of postseismic or interseismic deformation [e.g., *Johnson and Segall*, 2004; *Johnson et al.*, 2009; *Rousset et al.*, 2012; *Rollins et al.*, 2015]. Yet many important sources of off-fault deformation, such as viscoelasticity, thermoelasticity, and poroelasticity, cannot be easily represented in the earthquake cycle.

Viscoelastic relaxation is often considered a delayed stage of postseismic deformation, becoming more significant only after long-term (several years) deformation, and has been ignored altogether in many studies. However, more recent findings have suggested a prevalence of viscoelastic deformation much earlier during the postseismic period [*Sun et al.*, 2014; *DeVries and Meade*, 2016]. Several authors have explored the role of viscoelastic mantle flow in kinematically imposed earthquake cycles [e.g., *Kato*, 2002; *Johnson and Segall*, 2004; *Hetland and Hager*, 2005; *Takeuchi and Fialko*, 2013], but the full coupling between fault processes and off-fault deformation is missing. In this work, we present an integral method for simulating earthquake cycles that incorporates the nonlinear dynamics of fault slip and off-fault viscoelastic strain within the lithosphere-asthenosphere system in a consistent framework.

Our method can resolve all phases of the earthquake cycle, with slow-slip events and earthquakes emerging spontaneously from the nonlinear dynamics. To illustrate these concepts, we consider the two-dimensional antiplane shear problem where we couple the evolution of slip along two parallel, vertical strike-slip faults contained within a brittle elastic half-space along with viscoelastic strain beneath the brittle-ductile transition. In order to incorporate the dynamics of fault slip as well as off-fault strain we implement new elastostatic solutions for the stress and displacement fields due to distributed strain within a finite rectangular volume.

We examine the interactions of fault mechanics with those of the underlying medium, the evolution of slip and strain in the lithosphere-asthenosphere system throughout earthquake sequences, and the contribution

to postseismic surface displacement from viscoelastic flow. Our results suggest that viscoelastic relaxation may follow both slow-slip events and earthquakes alike and that viscoelastic flow can play a substantial role in early postseismic (<1 year) deformation, depending on the magnitude of the event and the rheology of the viscous substrate. The approach opens the door to even more sophisticated models that include dynamic feedbacks between localized and distributed deformation.

2. Model Description

Our model considers a classic two-dimensional antiplane problem incorporating two infinitely long, vertical strike-slip faults. The model plane is centered on a cross section of the two parallel faults, which are separated by a distance of 50 km and confined in a homogeneous half-space. In this framework, variation in slip occurs only with depth along both faults. We will refer to the two faults as the western and eastern faults (Figure 1). Both faults extend from the surface to the brittle-ductile transition at 35 km, with friction governed in a rate and state framework.

We incorporate two faults in the model in order to investigate the significance of earthquake magnitude with respect to postseismic viscous flow in a single simulation. The two faults are identical in size and physical properties, with the exception of the extent of their seismogenic zone, which controls the stability of fault slip and the potential magnitude of their seismic ruptures [*Jiang and Lapusta*, 2016]. For the western fault, a region of velocity-weakening friction ranges between depths of 5 and 15 km with velocity-strengthening properties extending at either side toward the free surface and the brittle-ductile transition. The eastern fault has a larger seismogenic region extending from 3 to 20 km depth.

Off-fault viscoelasticity beneath the brittle-ductile transition (35 km) is governed by power law dislocation creep, incorporating a depth-dependent thermal profile and confining pressure. The fault is loaded with a plate velocity of $V_{\text{pl}} = 31.5$ mm/yr and viscoelastic flow is driven with a strain rate of $\dot{\epsilon}_{12}^{0} = 10^{-14}$/s. We choose spatially uniform loading rates to enforce long-term, kinematically consistent models. Other scenarios with $V_{\text{pl}} = 0$, which are ignored here, correspond to faults driven from mantle flow alone. Further descriptions of the friction law and viscoelastic model are provided in the subsequent sections.

We study the evolution of deformation over earthquake cycles including frictional sliding along each fault and viscoelastic strain in the underlying medium. We use the integral method where the volume is discretized into finite elements with two depth-dependent fault meshes and a two-dimensional mesh corresponding to the viscoelastic material. The fault meshes consists of 120 uniform elements over the length of each fault. The two-dimensional mesh covers a domain from −300 to 300 km horizontally and 35 to 278 km at depth. The east and west faults are located at −25 and 25 km, respectively, within the coordinate system of the two-dimensional mesh. The grid contains 50×50 elements centered horizontally on the two faults. A window in which the horizontal width of the cells is uniform is set between −50 and 50 km. However, for computational efficiency the mesh for the viscoelastic material uses nonuniform elements, increasing in dimensions with distance from the fault system at depth as well as horizontally outside of this window.

We calculate the stress interactions among the fault and shear zone elements with analytic solutions for both displacements and distributed shear caused by viscoelastic deformation of a finite element (see Appendix A). The evolution of stress, as well as slip rate, strain rate, and the frictional state parameter is solved numerically using the integral method over numerous earthquake cycles. The advantage of the integral method over the classic finite element or spectral element methods lies in the numerical complexity. Whereas the discretization of the domain in finite elements leads to an algebraic problem solved in $O(N^3)$ operations [e.g., *Hearn et al.*, 2002; *Freed et al.*, 2006; *Kaneko et al.*, 2011; *Takeuchi and Fialko*, 2013], where N is the number of elements, the integral method uses $O(N^2)$ operations. In our two-dimensional case, with $N = 2740$, the integral method is 4 orders of magnitude faster, facilitating the evaluation of more detailed numerical models of deformation in the lithosphere-asthenosphere system. It is necessary to resolve a wide temporal range over earthquake cycles, varying between slow loading rates of millimeters per year to rapid coseismic slip rates on the order of meters per second. We solve for the time series using the fourth/fifth order accurate Runge Kutta method with adaptive time steps to optimize calculations based on the computational complexity at various stages of the earthquake cycle.

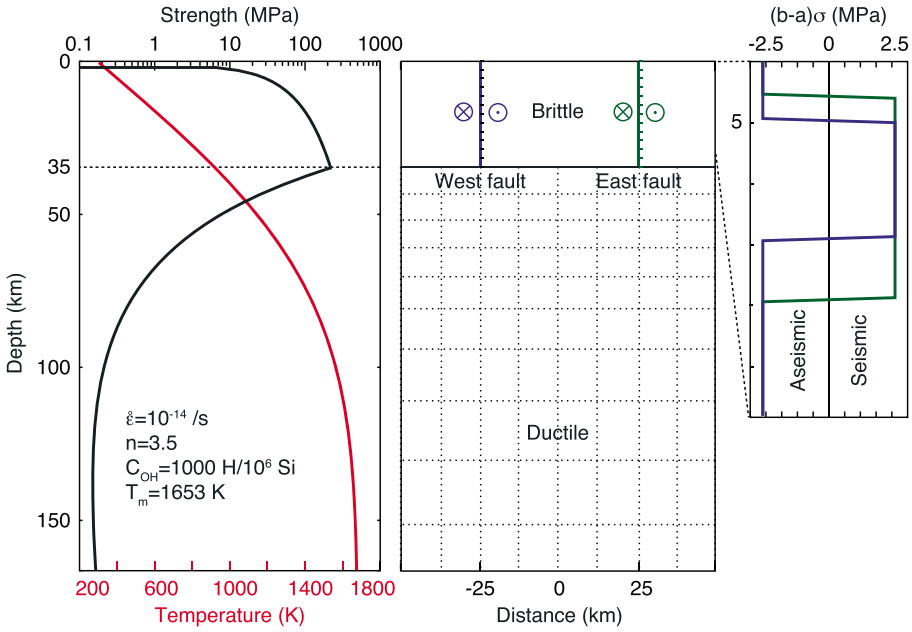

Figure 1. Model schematic for two-dimensional antiplane lithosphere-asthenosphere system. In the center is the spatial distribution in antiplane for the west and east faults, located at −25 and 25 km, respectively, and the ductile patches beneath the brittle-ductile transition at 35 km depth. The left box shows the depth-dependent thermal and strength profiles for defining the rheology, and the right box shows the extent of the seismogenic zones of the two faults.

2.1. Rate- and State-Dependent Fault Friction

Slip along the fault interfaces is governed with a Dieterich-Ruina rate and state friction law [*Dieterich*, 1979; *Ruina*, 1983]. The rate-and-state framework allows the simulation of all phases of slip evolution including the spontaneous emergence of creep, slow-slip events, and seismic ruptures [*Barbot et al.*, 2012; *Veedu and Barbot*, 2016]. The approach allows a full coupling between the brittle lithosphere and its underlying viscoelastic substrate, as opposed to only prescribed cycles of earthquakes [*Savage and Prescott*, 1978; *Johnson and Segall*, 2004; *Hetland and Hager*, 2005]. We use the following form,

$$\mu(V,\psi) = a \sinh^{-1}\left(\frac{V}{2V_0}\exp\left(\frac{\mu_0 + b\psi}{a}\right)\right) \tag{1}$$

$$\dot{\psi} = \frac{V_0 e^{-\psi} - V}{L} \tag{2}$$

where $\psi = \log(\frac{V_0\theta}{L})$. Here a is the direct-effect parameter, b is the state-evolution parameter, μ_0 is the coefficient of static friction, θ is the state variable, V is the slip velocity, V_0 is the reference slip velocity, and L is the characteristic weakening distance [*Lapusta and Barbot*, 2012]. We use the simplification that $\sinh^{-1}(x) = \log(x + \sqrt{x^2+1}) \approx \log(\gamma x + 1)$, where $1 \le \gamma \le 2$. Instead of solving for the inertial contribution directly, we incorporate radiation damping as an approximation at seismic velocities [*Rice et al.*, 2001]. The fault strength, τ, which is equal to the shear stress acting on the fault, is then

$$\tau = a\sigma \log\left[\frac{\gamma V}{2V_0}\exp\left(\frac{\mu_0 + b\psi}{a}\right) + 1\right] + \frac{GV}{2V_s} \tag{3}$$

where σ is the normal stress on the fault. By rearranging equation (3) one finds the following relation for the sliding rate,

$$\frac{GV'}{2V_s\gamma a\sigma}\exp\left(\frac{GV'}{2V_s\gamma a\sigma}\right) = \frac{GV_0}{V_s\gamma a\sigma}\exp\left(\frac{\tau + \frac{GV_0}{\gamma V_s}\exp\left(-\frac{\mu_0+b\psi}{a}\right) - \mu_0\sigma - b\psi\sigma}{a\sigma}\right) \tag{4}$$

where $V' = \gamma V + 2V_0 \exp\left(-\frac{\mu_0 + b\psi}{a}\right)$. We then make use of the Lambert W function to approximate the slip rate.

$$V = \frac{2a\sigma V_s}{G} W\left[\frac{GV_0}{\gamma a\sigma V_s} \exp\left(\frac{\tau + \frac{GV_0}{\gamma V_s}\exp\left(-\frac{\mu_0+b\psi}{a}\right) - \mu_0\sigma - b\psi\sigma}{a\sigma}\right)\right] - \frac{2V_0}{\gamma}\exp\left(-\frac{\mu_0 + b\psi}{a}\right) \quad (5)$$

For this work, we use a high-velocity approximation and set $\gamma = 2$. Slip events nucleate over a characteristic width h^* controlled by the characteristic weakening distance and effective confining pressure [*Ruina*, 1983]. We choose our fault sampling to resolve the nucleation size by a factor of 10 [*Lapusta and Liu*, 2009]. For consistency, we construct the mesh size for the surrounding volume to be identical in regions of homogenous sampling. In addition, we conduct resolution tests to verify numerical convergence.

Note that the rate and state friction law only includes logarithmic velocity weakening, whereas experimental evidence reveals the presence of stronger weakening taking place at high slip rates [*Rice*, 2006; *Dunham et al.*, 2011]. This stronger weakening is thought to be attributed to thermal softening from flash heating or local melting at asperity contacts [*Di Toro et al.*, 2004; *Nakatani*, 2001; *Nagata et al.*, 2012; *King and Marone*, 2012]. We do not address these thermal effects in this study; however, they may have substantial influence on rupture characteristics and are a topic for future studies.

2.2. Viscoelastic Deformation

We discretize the volume beneath the brittle-ductile transition as elementary rectangular patches, which we will refer to as shear zones. The off-fault medium is treated as a nonlinear viscoelastic material governed by dislocation creep [*Bürgmann and Dresen*, 2008]. The rheological behavior for the material then provides a power law dependence of the strain rate tensor $\dot{\epsilon}_{ij}$ and deviatoric stress σ'_{ij} of the form [*Karato and Jung*, 2003; *Hirth and Kohlstedt*, 2003]

$$\dot{\epsilon}_{ij} = A\tau^{n-1}\left(C_{OH}\right)^r \exp(\alpha\phi)\exp\left(-\frac{Q + \sigma\Omega}{RT}\right)\sigma'_{ij} \quad (6)$$

where A is a reference strain rate, τ is the norm of the deviatoric stress, n is the stress exponent, C_{OH} is the water fugacity, r is the water fugacity exponent, ϕ is the melt fraction, α is a constant, Q is the activation energy, σ is the confining pressure, Ω is the activation volume, R is the gas constant, and T is the absolute temperature. Values for the rheological parameters are used for wet dislocation creep conditions for olivine as determined from laboratory studies [*Hirth and Kohlstedt*, 2003]. In this study we ignore the presence of partial melt and set $\phi = 0$.

For the two-dimensional antiplane problem we consider the two strain components, ϵ_{12} and ϵ_{13}, and the corresponding shear stress components, τ_{12} and τ_{13}. Strain in the $\mathbf{e}_1 \otimes \mathbf{e}_3$ direction results in shear in the $\mathbf{e}_1 \otimes \mathbf{e}_2$ direction and vice versa; therefore, both stress components contain contributions from ϵ_{12} and ϵ_{13}. At each time step within the simulation we first calculate the strain rate components $\dot{\epsilon}_{12}$ and $\dot{\epsilon}_{13}$ attributed to dislocation creep from the current stress of τ_{12} and τ_{13}. We then determine the differential strain rates by subtracting the steady state strain rates required to maintain the initial strength profile, discussed in the following section. We convolve these with stress kernels to determine the corresponding stress rates everywhere in the volume due to strain in the shear zones (see Appendix A). The total stress rate on each shear zone, $\dot{\tau}_{12}$ and $\dot{\tau}_{13}$, and on the west and east faults, $\dot{\tau}_W$ and $\dot{\tau}_E$, is a linear combination of the individual slip and strain rates convolved with their respective stress kernels for slip and distributed strain.

$$\dot{\tau}_j = K^j_W(V_W - V_{\text{pl}}) + K^j_E(V_E - V_{\text{pl}}) + K^j_{12}\left(\dot{\epsilon}_{12} - \dot{\epsilon}^0_{12}\right) + K^j_{13}\left(\dot{\epsilon}_{13} - \dot{\epsilon}^0_{13}\right) \quad (7)$$

Here $j = \{W, E, 12, 13\}$ for stress induced on the west and east faults, and the $\dot{\tau}_{12}$ and $\dot{\tau}_{13}$ components of each shear zone, respectively. This method should scale naturally to three-dimensional deformation as the corresponding solutions for the stress kernels are developed.

2.3. Initial Conditions and Model Parameters

For the lithosphere-asthenosphere system we assume a simple "crème-brûlée" structure with a brittle layer overlaying a weak upper mantle [*Jackson*, 2002]. We apply a depth-dependent confining pressure $\sigma = \rho g z$, where z is the depth beneath the free surface, ρ is the material density, and g is the acceleration

Table 1. Model Parameters for Lithosphere-Asthenosphere Dynamics[a]

Parameter	Symbol	Value
Fault parameters		
Shear modulus	G	30 GPa
Fault strength	τ_F	200 MPa
Static friction coefficient	μ_0	0.2
Direct effect parameter	a	1×10^{-3}
Evolution effect parameter	b	1.21×10^{-3} (velocity strengthening)
		7.9×10^{-4} (velocity weakening)
Characteristic weakening distance	L	0.012 m
Plate rate	V_{pl}	10^{-9} m/s
Reference slip velocity	V_0	10^{-6} m/s
Shear wave speed	V_s	10^3 m/s
Rheological parameters		
Reference strain rate	A	90 (MPa s)$^{-1}$
Power law exponent	n	3.5
Activation energy	Q	530 kJ/mol
Activation volume	Ω	15×10^{-6} m^3/mol
Melt fraction	ϕ	0
Water fugacity	C_{OH}	1000 H/10^6 Si
Water fugacity exponent	r	1.2
Density	ρ	3300 kg/m^3
Thermal diffusivity	K	8×10^{-7} m/s^2
Plate age	t_{plate}	64 Ma
Basal mantle temperature	T_m	1380°C
Driving strain rate	$\dot{\epsilon}^0_{12}$	10^{-14} s^{-1}
	$\dot{\epsilon}^0_{13}$	0 s^{-1}

[a]Rheological parameters used from laboratory studies for wet dislocation creep conditions in olivine [*Hirth and Kohlstedt*, 2003].

due to gravity. The thermal model is based on a cooling half-space model with thermal diffusion from the basal mantle temperature $T_m = 1380°C$,

$$T(z) = T_m erf\left(\frac{z}{\sqrt{4Kt_{\text{plate}}}}\right) \tag{8}$$

where the plate age, t_{plate}, is taken to be 64 Ma and K is the thermal diffusivity. We ignore the adiabatic mantle temperature gradient, as its effect is most pronounced in deeper regions than considered in the model. The brittle-ductile transition is determined as the intersection of the brittle strength $\mu\sigma$ and the shear stress associated with a driving strain rate of $\dot{\epsilon}_{12} = 10^{-14}$ s^{-1} for dislocation creep. We then apply a uniform strength τ_F along the fault corresponding to the strength at the transition zone. As we ignore the thermal feedback effects on the fault, the static strength of the fault does not impact the dynamics of modeled fault slip. The model setup is shown in Figure 1, and values for model parameters are shown in Table 1.

3. Results

We simulate the evolution of slip and strain over multiple earthquake cycles for the lithosphere-asthenosphere system. Figure 2 displays time series covering 400 years of ruptures on the west and east faults as well as the ductile flow along the depth projection in between the two faults at $x_2 = 0$. Figure 2a shows the slip and strain rate as a function of time and depth, whereas Figure 2b is a function of the individual computational time steps, which range in duration on the order of 1 ms to 1 year throughout each earthquake cycle.

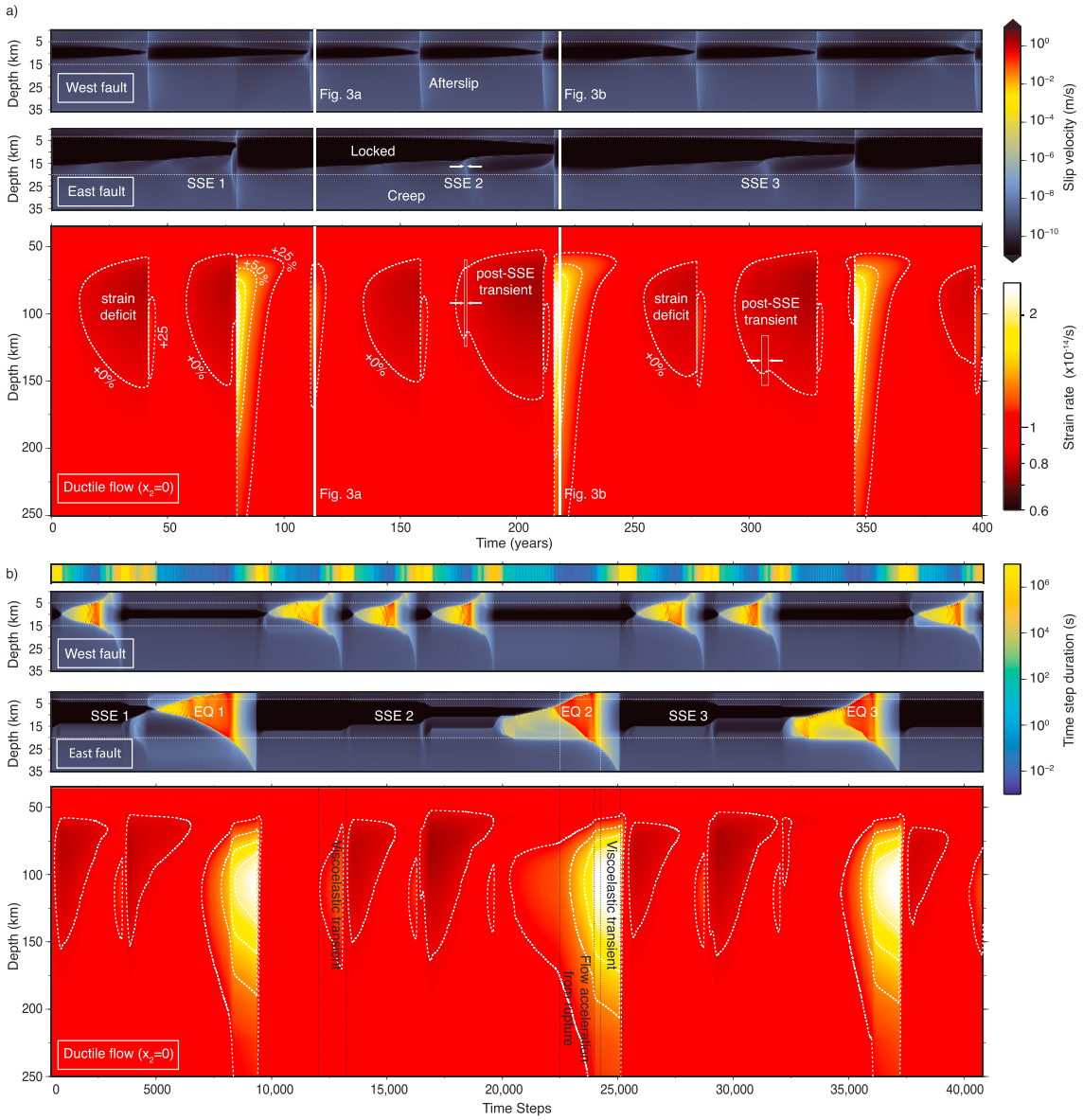

Figure 2. Time series of deformation evolution for the lithosphere-asthenosphere system over 400 years with 10 earthquakes and 3 slow-slip events. The evolution of slip and strain rates is shown as a function of (a) depth and time as well as (b) an individual computational time steps. The horizontal white bars indicate the limits of the velocity-weakening region. The horizontal white bars indicate the temporal location of the snapshots in Figure 3. Velocity-strengthening areas experience creep and afterslip. Velocity-weakening areas exhibit slow-slip events and earthquakes. Vertical black bars indicate periods of flow acceleration or viscoelastic transients.

Visualizing the time series in the time step domain highlights the propagation of the individual ruptures as well as the corresponding viscoelastic response. The radiation damping approximation neglects the delay incurred by the propagation of seismic waves to the mantle so an additional delay on the order of tens of seconds would be expected for mantle flow. In Figure 2b it is apparent that flow acceleration may begin early in the postseismic period, within minutes of the coseismic event. This agrees with *Sun et al.* [2014], who found that the onset of viscoelastic relaxation occurred during the early postseismic period of the 2011 Tohoku-oki earthquake. Our simulations show that viscoelastic relaxation may follow slow-slip events, which to date has not been confirmed observationally, presumably owed to its lesser magnitude compared to that following large earthquakes. Figure 2a also shows that high strain rates following each rupture persist within the first half of the subsequent earthquake cycle, which is in agreement with the kinematically consistent models of viscoelastic stress evolution of *DeVries and Meade* [2016]. However, for our model high strain rates occur even

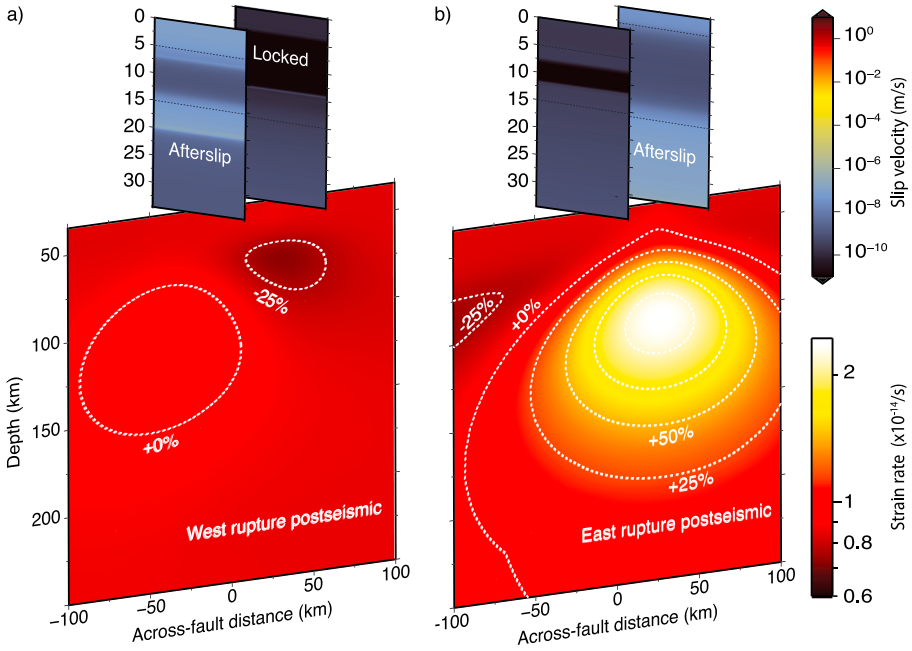

Figure 3. Spatial cross section of slip velocity and strain rate at temporal points showed in Figure 2 during the postseismic period following ruptures on the (a) west and (b) east faults. The degree of strain acceleration depends on the magnitude of the event. Strain deficit representing as little as 70% of plate rate accumulates late in the earthquake cycle.

earlier, within the first quarter of the earthquake cycle, presumably due to our specific choice for the nonlinear rheology. This suggests an early onset of viscoelastic deformation during the postseismic period.

In Figure 3 we show the spatial distribution of the strain rate as well as the slip velocity distribution on both faults at fixed time steps within the postseismic periods following ruptures on the west (Figure 3a) and east (Figure 3b) faults. For large ruptures, such as those generated on the east fault, the strain rate is potentially accelerated to over twice that of the driving strain rate. We also see the accumulation of a strain deficit within the shear zones beneath the faults prior to slip events. The reduction in strain rate occurs generally within

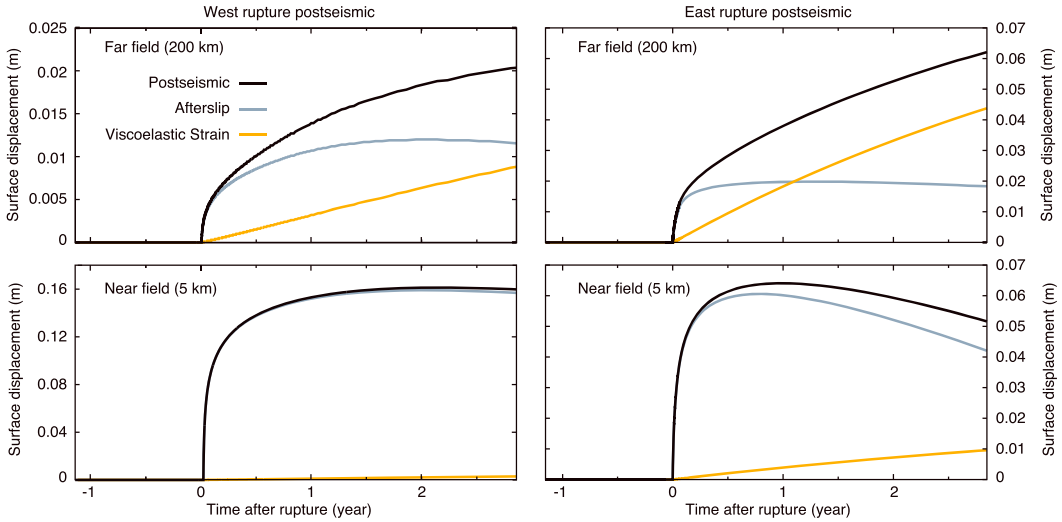

Figure 4. Postseismic surface displacement following (left column) west and (right column) east ruptures. Contributions are shown for (top row) far-field and (bottom row) near-field locations. The trend of surface displacement 1 year before the rupture has been modeled out.

the same region that is later accelerated during the seismic event, similar to how the seismogenic zone of the faults accrues a slip deficit prior to earthquakes. Long periods of strain deficit in the mantle have also been observed late in the earthquake cycle [*Kato*, 2002]; however, such models do not exhibit features such as slow-slip events and strain localisation which are only accommodated by nonlinear fault and mantle dynamics. A movie displaying the evolution of postseismic surface deformation as well as the spatial distributions of slip velocity and strain rate over 400 years can be found in the supporting information.

Figure 4 shows the postseismic surface deformation trends following ruptures on the west (left column) and east (right column) faults. Figure 4 (top row) shows deformation at far-field points 200 km from each fault whereas examples of near-field deformation are shown in Figure 4 (bottom row). As expected, near-field surface deformation is heavily dominated by afterslip for both west and east style ruptures. However, we see comparable contributions from viscoelastic strain and afterslip to far-field surface deformation from large earthquakes such as those on the east fault within the first year following the rupture. Even for smaller earthquakes, such as those on the west fault, viscoelastic strain can produce a considerable contribution, around 20%, to the total surface displacement within the first year following the rupture. The degree of surface displacement due to viscoelastic relaxation is comparable with similar studies using kinematically imposed slip models with nonlinear mantle rheologies [*Takeuchi and Fialko*, 2013]. Our framework, however, treats the afterslip contribution self-consistently.

4. Conclusions

We present a method for simulating earthquake cycles coupling both fault slip and viscoelastic strain within the lithosphere-asthenosphere system. The method overcomes many important limitations associated with kinematically imposed earthquakes cycles [e.g., *Kato*, 2002; *Johnson and Segall*, 2004; *Takeuchi and Fialko*, 2013], allowing us to incorporate all phases of the earthquake cycle in a consistent framework including nonlinear dynamics and spatial variations of inelastic properties for fault slip and distributed deformation. We examine the role of viscoelastic deformation in postseismic surface displacements and find that the acceleration of viscous flow can occur at the early onset of postseismic deformation, depending on the size of the rupture and the rheology of the asthenosphere. Viscoelastic deformation may play a substantial role for early postseismic studies following large earthquakes, limiting the appeal of pure afterslip models in geodetic studies. Our simulations also reveal the potential occurrence of viscoelastic transients following slow-slip events. As these occasionally reach large equivalent geodetic moments and magnitudes in nature (some as high as $M_w = 7.5$ [*Beroza and Ide*, 2011]), they may also be used to study the rheology of the viscoelastic substrate.

In this model, we do not address the dynamics of rheological parameters such as temperature, water fugacity or grain size. In particular, the thermal gradient, which contributes to governing viscoelastic creep, is assumed to remain at equilibrium. However, shear heating from seismic events may introduce localized variations in viscosity throughout seismic cycles that may modulate the viscoelastic response. In addition, we assume that the rheology is dominated by dislocation creep; however, the relative roles of diffusion and dislocation creep are not well understood and the relationship is highly dependent on the evolution of grain size. The proposed framework may be used as a basis to investigate remaining important questions such as the role of viscoelastic flow on earthquake clustering and triggering [e.g., *Freed and Lin*, 2001], and the development of mylonite shear zones at the deep extension of faults [e.g., *Takeuchi and Fialko*, 2013]. Incorporating the dynamics of distributed deformation in earthquake cycle modeling may provide greater insight into the physics of plate boundary deformation.

Appendix A: Two-Dimensional Antiplane Solutions

In order to account for the displacement and stresses imposed by distributed deformation we introduce two-dimensional antiplane elastostatic solutions for distributed strain occurring in an elementary rectangular volume. Considering an infinitely long and vertical shear region with strike in the x_1 direction, we define a two-dimensional rectangular area of thickness T and width W in the x_2 and x_3 directions, respectively. In antiplane $\partial/\partial x_1 = 0$ and $u_2 = u_3 = 0$. The deformation due to a displacement discontinuity can be represented by equivalent body forces arising from transformational (or eigen) strain [*Barbot and Fialko*, 2010, 2010]. In antiplane strain, the spatial distribution of eigenstrain can be represented using the Dirac's delta

function $\delta(\mathbf{x}) = \delta(x_1)\delta(x_2)\delta(x_3)$ and the boxcar function $\Pi(x)$, with the derivative $\Pi'(x) = \delta(x+1/2)-\delta(x-1/2)$ [*Barbot et al.*, 2008]. The eigenstrain is then given by

$$\begin{aligned}\epsilon^v_{12}(\mathbf{x}) &= \epsilon^v_{12}\,\Pi\left(\frac{x_2}{T}\right)\Pi\left(\frac{x_3}{W}\right)\\ \epsilon^v_{13}(\mathbf{x}) &= \epsilon^v_{13}\,\Pi\left(\frac{x_2}{T}\right)\Pi\left(\frac{x_3}{W}\right)\end{aligned} \tag{A1}$$

The deformation in the plane due to elastic coupling can be attributed to equivalent body forces

$$\begin{aligned}\mathbf{f} &= -\nabla\cdot\left(\mathbf{C}:\epsilon^v\right)\\ &= -2G\left[\epsilon^v_{12,2}+\epsilon^v_{13,3}\right]\mathbf{e}_1\end{aligned} \tag{A2}$$

So we have the equivalent body forces

$$\begin{aligned}f_1 = 2G\Big[&\epsilon^v_{12}\frac{1}{T}\left(\delta\left(\frac{x_2}{T}-\frac{1}{2}\right)-\delta\left(\frac{x_2}{T}+\frac{1}{2}\right)\right)\Pi\left(\frac{x_3}{W}\right)\\ &+\epsilon^v_{13}\,\Pi\left(\frac{x_2}{T}\right)\frac{1}{W}\left(\delta\left(\frac{x_3}{W}-\frac{1}{2}\right)-\delta\left(\frac{x_3}{W}+\frac{1}{2}\right)\right)\Big]\end{aligned} \tag{A3}$$

with $f_2 = f_3 = 0$. From conservation of momentum $\sigma_{12,2}+\sigma_{13,3}+f_1 = 0$, therefore, $G(u_{1,22}+u_{1,33})+f = 0$. The displacement field in the plane can then be obtained by solving Poisson's equation.

$$\nabla^2 u_1 + \frac{1}{G}f_1 = 0 \tag{A4}$$

From successive integration the solution to Poisson's equation for a point source $\nabla^2 u_1 = \delta(\mathbf{x})$ can be written as

$$u_1(x_2,x_3) = \frac{1}{4\pi}\ln\left({x_2}^2+{x_3}^2\right) \tag{A5}$$

To consider the effect of a free surface at $x_3 = 0$, we use the method of images, whereby any source in $x_3 > 0$ is paired by an image at $-x_3$ with the same force orientation in the $\mathbf{e}_1$ direction. The displacement in the plane due to imposed shear strain in the rectangle is

$$\begin{aligned}u_1(x_2,x_3) = &-\frac{1}{4\pi G}\int_{-\infty}^{\infty} f_1(y_2,y_3)\ln\left((x_2-y_2)^2+(x_3-y_3)^2\right)\mathrm{d}y_2\mathrm{d}y_3\\ &-\frac{1}{4\pi G}\int_{-\infty}^{\infty} f_1(y_2,y_3)\ln\left((x_2-y_2)^2+(x_3+y_3)^2\right)\mathrm{d}y_2\mathrm{d}y_3\end{aligned} \tag{A6}$$

We set the rectangular area beneath the free surface such that the eigenstrain is applied between the depth D and $D+W$ and centered on (y_2, y_3). The total displacement field incorporates contributions from both strain components ϵ^v_{12} and ϵ^v_{13}.

$$u_1(x_2,x_3) = J_{12}+K_{12}+J_{13}+K_{13} \tag{A7}$$

The integrals are given in explicit form below. They involve the distances to the four corners of the rectangular area and their image

$$\begin{aligned}J_{12} = \frac{\epsilon^v_{12}}{2\pi}\Big[&\left(x_3-D-W\right)\ln\left((x_2-T/2)^2+(x_3-D-W)^2\right)\\ &-\left(x_3-D-W\right)\ln\left((x_2+T/2)^2+(x_3-D-W)^2\right)\\ &-\left(x_3-D\right)\ln\left((x_2-T/2)^2+(x_3-D)^2\right)\\ &+\left(x_3-D\right)\ln\left((x_2+T/2)^2+(x_3-D)^2\right)\\ &+2\left(x_2-T/2\right)\left(\arctan\frac{x_3-D-W}{x_2-T/2}-\arctan\frac{x_3-D}{x_2-T/2}\right)\\ &+2\left(x_2+T/2\right)\left(\arctan\frac{x_3-D}{x_2+T/2}-\arctan\frac{x_3-D-W}{x_2+T/2}\right)\Big]\end{aligned} \tag{A8}$$

$$
\begin{aligned}
J_{13} = \frac{\epsilon^v_{13}}{2\pi}\Big[& (x_2 - T/2)\ln\left((x_2 - T/2)^2 + (x_3 - D - W)^2\right) \\
& - (x_2 + T/2)\ln\left((x_2 + T/2)^2 + (x_3 - D - W)^2\right) \\
& - (x_2 - T/2)\ln\left((x_2 - T/2)^2 + (x_3 - D)^2\right) \\
& + (x_2 + T/2)\ln\left((x_2 + T/2)^2 + (x_3 - D)^2\right) \\
& + 2(x_3 - W - D)\left(\arctan\frac{x_2 - T/2}{x_3 - D - W} - \arctan\frac{x_2 + T/2}{x_3 - D - W}\right) \\
& + 2(x_3 - D)\left(\arctan\frac{x_2 + T/2}{x_3 - D} - \arctan\frac{x_2 - T/2}{x_3 - D}\right)\Big]
\end{aligned} \tag{A9}
$$

The terms K_{12} and K_{13} come from the method of images.

$$
\begin{aligned}
K_{12} = \frac{\epsilon^v_{12}}{2\pi}\Big[& (x_3 + D + W)\ln\left((x_2 + T/2)^2 + (x_3 + D + W)^2\right) \\
& - (x_3 + D + W)\ln\left((x_2 - T/2)^2 + (x_3 + D + W)^2\right) \\
& - (x_3 + D)\ln\left((x_2 + T/2)^2 + (x_3 + D)^2\right) \\
& + (x_3 + D)\ln\left((x_2 - T/2)^2 + (x_3 + D)^2\right) \\
& + 2(x_2 + T/2)\left(\arctan\frac{x_3 + D + W}{x_2 + T/2} - \arctan\frac{x_3 + D}{x_2 + T/2}\right) \\
& + 2(x_2 - T/2)\left(\arctan\frac{x_3 + D}{x_2 - T/2} - \arctan\frac{x_3 + D + W}{x_2 - T/2}\right)\Big]
\end{aligned} \tag{A10}
$$

$$
\begin{aligned}
K_{13} = \frac{\epsilon^v_{13}}{2\pi}\Big[& (x_2 - T/2)\ln\left((x_2 - T/2)^2 + (x_3 + D + W)^2\right) \\
& - (x_2 + T/2)\ln\left((x_2 + T/2)^2 + (x_3 + D + W)^2\right) \\
& - (x_2 - T/2)\ln\left((x_2 - T/2)^2 + (x_3 + D)^2\right) \\
& + (x_2 + T/2)\ln\left((x_2 + T/2)^2 + (x_3 + D)^2\right) \\
& + 2(x_3 + D + W)\left(\arctan\frac{x_2 - T/2}{x_3 + D + W} - \arctan\frac{x_2 + T/2}{x_3 + D + W}\right) \\
& + 2(x_3 + D)\left(\arctan\frac{x_2 + T/2}{x_3 + D} - \arctan\frac{x_2 - T/2}{x_3 + D}\right)\Big]
\end{aligned} \tag{A11}
$$

The stress can be evaluated from the strain components $\epsilon_{12} = u_{1,2}/2$ and $\epsilon_{13} = u_{1,3}/2$, leading to the following stress components, $\sigma_{12} = G(u_{1,2} - \epsilon^v_{12})$ and $\sigma_{13} = G(u_{1,3} - \epsilon^v_{13})$.

$$
\begin{aligned}
\sigma_{12} = & \frac{G\epsilon^v_{13}}{2\pi}\Big[\ln\left((x_2 - T/2)^2 + (x_3 - D - W)^2\right) - \ln\left((x_2 + T/2)^2 + (x_3 - D - W)^2\right) \\
& + \ln\left((x_2 - T/2)^2 + (x_3 + D + W)^2\right) - \ln\left((x_2 + T/2)^2 + (x_3 + D + W)^2\right) \\
& - \ln\left((x_2 - T/2)^2 + (x_3 - D)^2\right) + \ln\left((x_2 + T/2)^2 + (x_3 - D)^2\right) \\
& - \ln\left((x_2 - T/2)^2 + (x_3 + D)^2\right) + \ln\left((x_2 + T/2)^2 + (x_3 + D)^2\right)\Big] \\
& + \frac{G\epsilon^v_{12}}{\pi}\Big[\arctan\frac{x_3 - D}{x_2 + T/2} - \arctan\frac{x_3 - D}{x_2 - T/2} \\
& + \arctan\frac{x_3 - D - W}{x_2 - T/2} - \arctan\frac{x_3 - D - W}{x_2 + T/2} \\
& - \arctan\frac{x_3 + D + W}{x_2 - T/2} - \arctan\frac{x_3 + D}{x_2 + T/2} \\
& + \arctan\frac{x_3 + D}{x_2 - T/2} + \arctan\frac{x_3 + D + W}{x_2 + T/2}\Big] \\
& - 2G\epsilon^v_{12}\Pi\left(\frac{x_2}{T}\right)\Pi\left(\frac{2x_3 - 2D - W}{2W}\right)
\end{aligned} \tag{A12}
$$

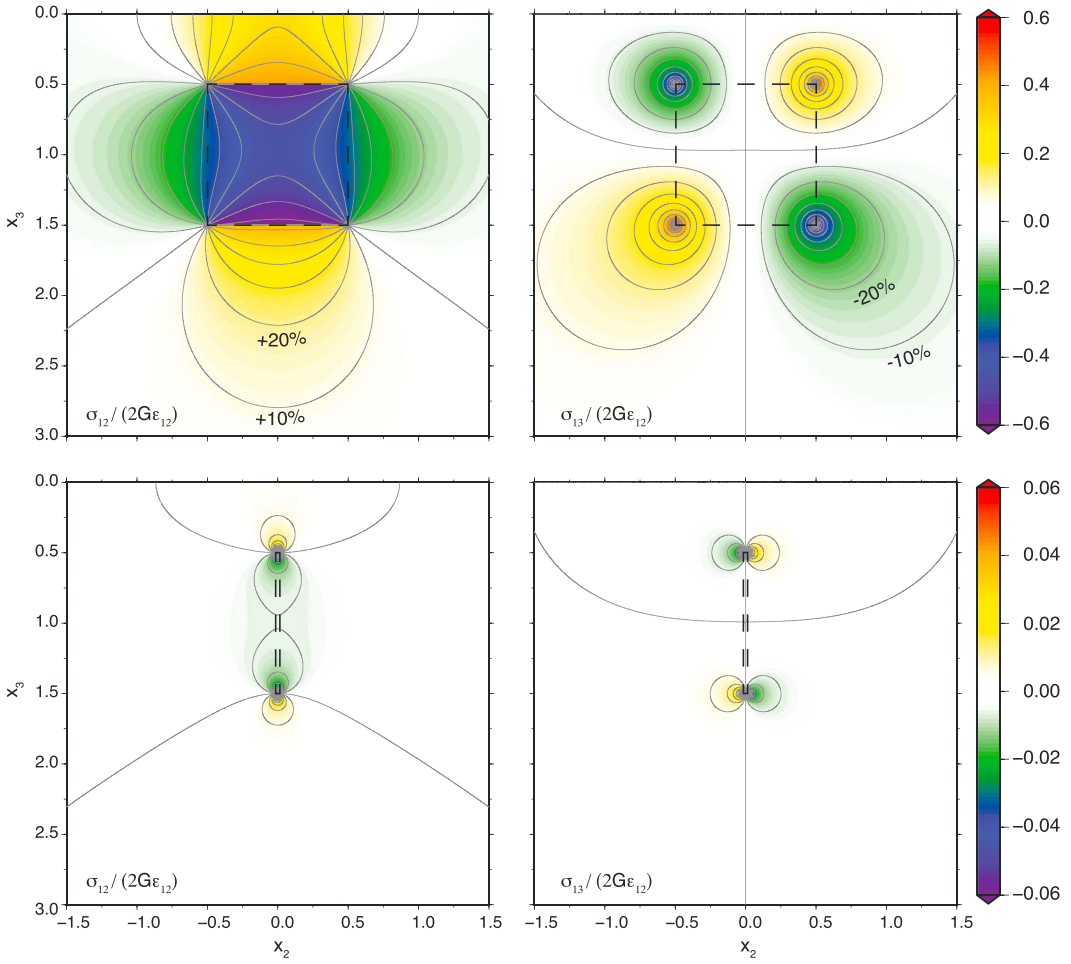

Figure A1. Stress fields corresponding to the (left column) σ_{12} and (right column) σ_{13} components due to distributed antiplane shear within a rectangular region of width $W = 1$ and thickness (top row) $T = W$ and (bottom row) $T = W/100$. The stress fields are generated with initial eigenstrain $\epsilon^v_{12} = 10^{-6}$.

Eigenstrain in the $\mathbf{e}_1 \otimes \mathbf{e}_3$ direction causes shear in the $\mathbf{e}_1 \otimes \mathbf{e}_2$ and vice versa.

$$
\begin{aligned}
\sigma_{13} = \frac{G\epsilon^v_{12}}{2\pi} & \left[\ln\left((x_2 - T/2)^2 + (x_3 - D - W)^2\right) - \ln\left((x_2 + T/2)^2 + (x_3 - D - W)^2\right)\right. \\
& - \ln\left((x_2 - T/2)^2 + (x_3 + D + W)^2\right) + \ln\left((x_2 + T/2)^2 + (x_3 + D + W)^2\right) \\
& - \ln\left((x_2 - T/2)^2 + (x_3 - D)^2\right) + \ln\left((x_2 + T/2)^2 + (x_3 - D)^2\right) \\
& \left. + \ln\left((x_2 - T/2)^2 + (x_3 + D)^2\right) - \ln\left((x_2 + T/2)^2 + (x_3 + D)^2\right)\right] \\
+ \frac{G\epsilon^v_{13}}{\pi} & \left[\arctan\frac{x_2 + T/2}{x_3 - D} - \arctan\frac{x_2 - T/2}{x_3 - D}\right. \\
& - \arctan\frac{x_2 + T/2}{x_3 - D - W} + \arctan\frac{x_2 - T/2}{x_3 - D - W} \\
& + \arctan\frac{x_2 + T/2}{x_3 + D} - \arctan\frac{x_2 - T/2}{x_3 + D} \\
& \left. + \arctan\frac{x_2 - T/2}{x_3 + D + W} - \arctan\frac{x_2 + T/2}{x_3 + D + W}\right] \\
-2G\,\epsilon^v_{13} & \Pi\left(\frac{x_2}{T}\right)\Pi\left(\frac{2x_3 - 2D - W}{2W}\right)
\end{aligned}
\tag{A13}
$$

These solutions provide a description of the displacement and stress caused by a rectangular volume under shear in the case of antiplane strain with a free surface. These are the main ingredients to solve for viscoelastic

deformation using the integral method. The solutions for distributed shear are closely related to those for slip constrained on a two-dimensional plane. As the thickness T of the shear zone becomes vanishingly small with respect to the other dimensions, the solutions converge to those of a fault, as shown in Figure A1 (bottom row).

Acknowledgments
The software used in this study is hosted at https://bitbucket.org/sbarbot/unicycle. This research was supported by the National Research Foundation of Singapore under the NRF Fellowship scheme (National Research Fellow Awards NRF-NRFF2013-04) and by the Earth Observatory of Singapore, the National Research Foundation, and the Singapore Ministry of Education under the Research Centres of Excellence initiative.

References

Ampuero, J. P., and A. M. Rubin (2008), Earthquake nucleation on rate and state faults—Aging and slip laws, *J. Geophys. Res.*, *113*, B01302, doi:10.1029/2007JB005082.

Barbot, S., N. Lapusta, and J. P. Avouac (2012), Under the hood of the earthquake machine: Toward predictive modelling of the seismic cycle, *Science*, *336*(6082), 708–710.

Barbot, S., Y. Fialko, and D. Sandwell (2008), Effect of a compliant fault zone on the inferred earthquake slip distribution, *J. Geophys. Res.*, *113*, B06404, doi:10.1029/2007JB005256.

Barbot, S., Y. Fialko, and Y. Bock (2009), Postseismic deformation due to the M_w 6.0 2004 Parkfield earthquake: Stress-driven creep on a fault with spatially variable rate-and-state friction parameters, *J. Geophys. Res.*, *114*, B07405, doi:10.1029/2008JB005748.

Barbot, S., and Y. Fialko (2010), Fourier-domain Green's function for an elastic semi-infinite solid under gravity, with applications to earthquake and volcano deformation, *Geophys. J. Int.*, *182*(2), 568–582.

Barbot, S., and Y. Fialko (2010), A unified continuum representation of postseismic relaxation mechanisms: Semi-analytic models of afterslip, poroelastic rebound and viscoelastic flow, *Geophys. J. Int.*, *182*(3), 1124–1140.

Beroza, G. C., and S. Ide (2011), Slow earthquakes and nonvolcanic tremor, *Ann. Rev. Earth Planet. Sci.*, *39*, 271–296.

Bürgmann, R., and G. Dresen (2008), Rheology of the lower crust and upper mantle: Evidence from rock mechanics, geodesy and field observations, *Ann. Rev. Earth Planet. Sci.*, *36*, 531–567.

DeVries, P. M. R., and B. J. Meade (2016), Kinematically consistent models of viscoelastic stress evolution, *Geophys. Res. Lett*, *43*, 4205–4214, doi:10.1002/2016GL068375.

Dieterich, J. H. (1979), Modeling of rock friction—1. Experimental results and constitutive equations, *J. Geophys. Res.*, *84*, 2161–2168, doi:10.1029/JB084iB05p02161.

Di Toro, G., D. L. Goldsby, and T. E. Tullis (2004), Friction falls towards zero in quartz rock as slip velocity approaches seismic rates, *Nature*, *427*, 436–439.

Dunham, E. M., D. Belanger, L. Cong, and J. E. Kozdon (2011), Earthquake ruptures with strongly rate-weakening friction and off-fault plasticity. Part 1: Planar faults, *Bull. Seismol. Soc. Am.*, *101*(5), 2296–2307.

Erickson, B. A., and E. M. Dunham (2014), An efficient numerical method for earthquake cycles in heterogeneous media: Alternating sub-basin and surface-rupturing events on faults crossing a sedimentary basin, *J. Geophys. Res. Solid Earth*, *119*(4), 3290–3316, doi:10.1002/2013JB010614.

Freed, A. M., and J. Lin (2001), Delayed triggering of the 1999 Hector Mine earthquake by viscoelastic stress transfer, *Nature*, *411*, 180–183.

Freed, A. M., et al. (2006), Implications of deformation following the 2002 Denali, Alaska, earthquake for postseismic relaxation processes and lithospheric rheology, *J. Geophys. Res.*, *111*, B01401, doi:10.1029/2005JB003894.

Hearn, E. H., R. Bürgmann, and R. E. Reilinger (2002), Dynamics of Izmit earthquake postseismic deformation and loading of the Düzce earthquake hypocenter, *Bull. Seismol. Soc. Am.*, *92*(1), 172–193.

Hetland, E. A., and B. H. Hager (2005), Postseismic and interseismic displacements near a strike-slip fault: A two-dimensional theory for general linear viscoelastic rheologies, *J. Geophys. Res.*, *110*, B10401, doi:10.1029/2005JB003689.

Hirth, G., and D. Kohlstedt (2003), Rheology of the upper mantle and the mantle wedge: A view from the experimentalists, *Geophys. Monogr.*, *138*, 83–105.

Hori, T., et al. (2004), A numerical simulation of earthquake cycles along the Nankai Trough in southwest Japan: Lateral variation in frictional property due to the slab geometry controls the slab geometry controls the nucleation position, *Earth Planet. Lett.*, *228*, 215–226.

Jackson, J. (2002), Strength of the continental lithosphere: Time to abandon the jelly sandwich?, *GSA Today*, *12*(9), 4–10.

Jiang, J., and N. Lapusta (2016), Deeper penetration of large earthquakes on seismically quiescent faults, *Science*, *352*(6291), 1291–1297.

Johnson, K. M., R. B. Bürgmann, and J. T. Freymueller (2009), Coupled afterslip and viscoelastic flow following the 2002 Denali Fault, Alaska earthquake, *Geophys. J. Int.*, *176*(3), 670–682.

Johnson, K. M., and P. Segall (2004), Viscoelastic earthquake cycle models with deep stress-driven creep along the San Andreas Fault system, *J. Geophys. Res.*, *109*, B10403, doi:10.1029/2004JB003096.

Kaneko, Y., J. P. Avouac, and N. Lapusta (2010), Towards inferring earthquake patterns from geodetic observations of inter seismic coupling, *Nat. Geosci.*, *3*, 363–369.

Kaneko, Y., J. P. Ampuero, and N. Lapusta (2011), Spectral-element simulations of long-term fault slip: Effect of low-rigidity layers on earthquake-cycle dynamics, *J. Geophys. Res.*, *116*, B10313, doi:10.1029/2011JB008395.

Karato, S-I., and H. Jung (2003), Effects of pressure on high-temperature dislocation creep in olivine, *Philos. Mag.*, *83*(3), 401–414.

Kato, N. (2002), Seismic cycle on a strike-slip fault with rate- and state-dependent strength in an elastic layer overlying a viscoelastic half space, *Earth Planets Space*, *54*, 1077–1083.

Kenner, S., and P. Segall (2000), A mechanical model for intraplate earthquakes: Application to the New Madrid seismic zone, *Science*, *289*(5488), 2329–2332.

King, D. S. H., and C. Marone (2012), Frictional properties of olivine at high temperature with applications to strength and dynamics of the oceanic lithosphere, *J. Geophys. Res.*, *117*, B12203, doi:10.1029/2012JB009511.

Lapusta, N., and S. Barbot (2012), Models of earthquakes and aseismic slip based on laboratory-derived rate-and-state friction laws, in *The Mechanics of Faulting: From Laboratory to Real Earthquakes*, edited by A. Bizzarri and H. S. Bhat, pp. 153–207, Research Signpost, Trivandrum, Kerala.

Lapusta, N., and Y. Liu (2009), Three-dimensional boundary integral modelling of spontaneous earthquake sequences and aseismic slip, *J. Geophys. Res.*, *114*, B09303, doi:10.1029/2008JB005934.

Lapusta, N., and J. Rice (2003), Nucleation and early seismic propagation of small and large events in a crustal earthquake model, *J. Geophys. Res.*, *108*(B4), 2205, doi:10.1029/2001JB000793.

Veedu, D. M., and S. Barbot (2016), The Parkfield tremors reveal slow and fast ruptures on the same asperity, *Nature*, *532*, 361–365.

Nagata, K., M. Nakatani, and S. Yoshida (2012), A revised rate- and state-dependent friction law obtained by constrained constitutive and evolution laws separately with laboratory data, *J. Geophys. Res.*, *117*, B02314, doi:10.1029/2011JB008818.

Nakatani, M. (2001), Conceptual and physical clarification of rate and state friction: Frictional sliding as a thermally activated rheology, *J. Geophys. Res.*, *106*, B713347, doi:10.1029/2000JB900453.

Okada, Y. (1985), Surface deformation due to shear and tensile faults in a half-space, *Bull. Seismol. Soc. Am.*, *75*, 1135–1154.
Okada, Y. (1992), Surface deformation due to shear and tensile faults in a half-space, *Bull. Seismol. Soc. Am.*, *82*, 1018–1040.
Rice, J. R., N. Lapusta, and K. Ranjith (2001), Rate and state dependent friction and the stability of sliding between elastically deformable solids, *J. Mech. Phys. Solids*, *49*, 1865–1898.
Rice, J. R. (2006), Heating and weakening of faults during earthquake slip, *J. Geophys. Res.*, *111*, B05311, doi:10.1029/2005JB004006.
Rollins, C., S. Barbot, and J. P. Avouac (2015), Post seismic deformation following the 2010 M_w = 7.2 El Mayor–Cucapah earthquake: Observations, kinematic inversions, and dynamic models, *Pure Appl. Geophys.*, *172*(5), 1305–1359.
Rousset, B., et al. (2012), Postseismic deformation following the 1999 Chi-Chi earthquake, Taiwan: Implication for lower-crust rheology, *J. Geophys. Res.*, *117*, B12405, doi:10.1029/2012JB009571.
Ruina, A. (1983), Slip instability and state variable friction laws, *J. Geophys. Res.*, *88*(B12), 10,359–10,370.
Savage, J. C., and W. H. Prescott (1978), Asthenosphere readjustment and the earthquake cycle, *J. Geophys. Res.*, *83*, 3369–3376.
Segall, P., and J. Davis (1997), GPS applications for geodynamics and earthquake studies, *Annu. Rev. Earth Planet. Sci.*, *25*, 301–336.
Sun, T., et al. (2014), Prevalence of viscoelastic relaxation after the 2011 Tohoku-oki earthquake, *Nature*, *514*, 84–87, doi:10.1038/nature13778.
Takeuchi, C., and Y. Fialko (2013), On the effects of thermally weakened ductile shear zones on postseismic deformation, *J. Geophys. Res. Solid Earth*, *118*(12), 6295–6310.